Energy & Environmental Science

ROYAL SOCIETY OF CHEMISTRY

PAPER

View Article Online
View Journal | View Issue

Cite this: *Energy Environ. Sci.*, 2021, **14**, 4095

Principles of interlayer-spacing regulation of layered vanadium phosphates for superior zinc-ion batteries†

Linfeng Hu, ‡*[ab] Zeyi Wu,‡[b] Chengjie Lu,[a] Fei Ye,[a] Qiang Liu[a] and Zhengming Sun [a]

Received 19th April 2021,
Accepted 26th May 2021

DOI: 10.1039/d1ee01158h

rsc.li/ees

Layered vanadium phosphate ($VOPO_4{\cdot}2H_2O$) is reported as a promising cathode material for rechargeable aqueous Zn^{2+} batteries (ZIBs) owing to its unique layered framework and high discharge plateau. However, its sluggish Zn^{2+} diffusion kinetics, low specific capacity and poor electrochemical stability remain major issues in battery application. In this work, a group of phenylamine (PA)–intercalated $VOPO_4{\cdot}2H_2O$ materials with varied interlayer spacing (14.8, 15.6 and 16.5 Å) is synthesized respectively *via* a solvothermal method for the cathode of aqueous ZIBs. The specific capacity is quite dependent on the *d*-spacing in the PA–$VOPO_4{\cdot}2H_2O$ system following an approximate linear tendency, and the maximum interlayer spacing (16.5 Å phase) results in a discharge capacity of 268.2 mA h g^{-1} at 0.1 A g^{-1} with a high discharge plateau of ~1.3 V and an energy density of 328.5 W h kg^{-1}. Both of the experimental data and DFT calculation identify that the optimal 16.5 Å spacing can boost fast zinc-ion diffusion with an ultrahigh diffusion coefficient of ~5.7×10^{-8} cm^{-2} s^{-1}. The intercalation of PA molecules also significantly increases the hydrophobility in the aqueous electrolyte, resulting in the inhibition of the decomposition/dissolution of $VOPO_4{\cdot}2H_2O$ and remarkably improved cycling stability over 2000 cycles at 5.0 A g^{-1} with a capacity retention of ~200 mA h g^{-1}. Our study provides a feasible solution for the sluggish Zn^{2+} diffusion kinetics and poor cyclic stability, and also shows a clear understanding of the interlayer chemistry principle of layered phosphates toward high-performance zinc-ion batteries.

Broader context

Rechargeable aqueous zinc-ion batteries (ZIBs) have attracted lots of attention in terms of green energy storage most recently. However, substantial revolution of aqueous ZIBs is still hindered by limited cathode performance with sluggish Zn^{2+} diffusion kinetics, low specific capacity and poor electrochemical stability. To promote the progress in practical application, the development of a novel cathode with superior ion-storage performance is urgently required. This work realizes a series of layered vanadium phosphate ($VOPO_4$) materials with tunable interlayer spacing (14.8, 15.6 and 16.5 Å) *via* controllable phenylamine (PA)-intercalation engineering. An approximate linear tendency between specific capacity and the regulated interlayer spacing is further revealed. In particular, the maximum interlayer spacing (16.5 Å) phase results in a considerable specific capacity of 268.2 mA h g^{-1} with a high plateau of ~1.3 V and thus an advantageous energy density of 328.5 W h kg^{-1}. Our finding provides clear guidance on the interlayer chemistry principle toward high-performance zinc-ion batteries.

1. Introduction

Nowadays, although rechargeable lithium-ion batteries (LIBs) are widely used for various portable electronics and electric vehicles, limited Li sources and severe safety issues are two main drawbacks of LIBs. With the rapid development of modern electronics and advanced equipment, beyond-lithium-ion (Na^+, K^+, Mg^{2+}, Ca^{2+}, Zn^{2+}, and Al^{3+}) batteries have recently attracted growing attention for energy storage systems.[1] Among them, zinc is an abundant metallic element in the earth's crust far exceeding Li. More importantly, rechargeable aqueous zinc-ion batteries (ZIBs) are based on an aqueous electrolyte, resulting in much superior safety to that of alkali metal (Li^+, Na^+, and K^+) based secondary batteries. Consequently, ZIBs have been considered as very promising

[a] *School of Materials Science and Engineering, Southeast University, Nanjing, 211189, China. E-mail: linfenghu@seu.edu.cn*
[b] *Department of Materials Science, Fudan University, Shanghai 200433, China*

† Electronic supplementary information (ESI) available. See DOI: 10.1039/d1ee01158h

‡ These authors contributed equally: Linfeng Hu and Zeyi Wu.

candidates for next-generation battery systems.[2,3] Nevertheless, the revolution of aqueous ZIBs is still at the early stage and far from the prospective applications, which is mainly limited by the absence of suitable cathode materials especially with high energy density and sufficiently long lifespan.[4] The origin of this issue should be ascribed to the intrinsic difference between univalent lithium ions and divalent zinc ions. Due to the similar radius of Li^+ (0.076 nm) and Zn^{2+} (0.074 nm), the surface charge density of divalent Zn^{2+} is more than twice that of Li^+, and the much stronger electrostatic interaction between Zn^{2+} and the lattice framework of the electrode materials thus leads to sluggish diffusion kinetics and even structure deterioration.[5,6]

Inorganic layered compounds, based on a typical layered structure and rich intercalation chemistry, have been particularly studied in metal-ion batteries. In particular, layered vanadium phosphate, $VOPO_4{\cdot}2H_2O$, has been reported as an important cathode material for ZIBs accompanied by a Zn^{2+} intercalation/de-intercalation mechanism in its interlayer galleries.[7–9] Remarkably, taking advantage of the enhanced ionicity of V–O bonds with the existence of PO_4^{3-}, layered $VOPO_4{\cdot}2H_2O$ exhibits a much higher discharge plateau (1.1–1.2 V) than other V-based cathode materials.[10–12] It should be emphasized that energy density is quite dependent on the discharge plateau of the cathode, and such a merit of layered $VOPO_4{\cdot}2H_2O$ is highly desirable to achieve a high energy density of ZIBs.[10] Unfortunately, the specific capacity and the rate capability of $VOPO_4{\cdot}2H_2O$-based ZIBs are still unsatisfactory due to the strong electrostatic interactions between Zn^{2+} and the $VOPO_4$ host with sluggish Zn^{2+} diffusion kinetics. On the other hand, the dissolution/decomposition behavior of $VOPO_4{\cdot}2H_2O$ in mild aqueous electrolyte generally results in very fast capacity/voltage fading during long-term cycling with a rather poor cyclic stability. Although the dissolution/decomposition issue has been addressed by PO_4^{3-} addition and high salt concentration of the aqueous electrolyte to shift the decomposition equilibrium and prevent dissolution,[9] the as-reported capacity of the $VOPO_4{\cdot}2H_2O$ cathode is still less than 170 mA h g^{-1}, which is much smaller than its theoretical specific capacity (>300 mA h g^{-1}). It is still a challenge to realize the superior performances for layered $VOPO_4{\cdot}2H_2O$ combining high discharge capacity, high rate capability and long cycling stability toward aqueous ZIBs applications.

Recent progress in lithium-/sodium-/magnesium-ion batteries unveils the interlayer spacing of layered materials as natural two-dimensional (2D) ion transport/diffusion channels.[13–16] In principle, increasing the interlayer spacing of a layered structure facilitates the ion transport by creating a lower energy barrier.[6,17,18] Superior sodium-ion battery performance should be explored from the layered materials with larger interlayer spacing.[19,20] Also, it is of great interest to obtain a fundamental understanding of the dependence of zinc-ion storage behaviour on interlayer spacing for layered $VOPO_4{\cdot}2H_2O$. However, there is still no report on the interlayer spacing modulation in layered vanadium phosphate for zinc-ion storage to date.

Herein, we found that the interlayer spacing of layered $VOPO_4{\cdot}2H_2O$ (VOP, 7.4 Å) can be successfully tuned by a phenylamine (PA) intercalated strategy through a facile solvothermal route. The crystal water in the $VOPO_4{\cdot}2H_2O$ was extracted from the interlayer space accompanied with the PA molecule intercalation. Three PA-intercalated $VOPO_4$ (labeled as PA–VOP) phases with identical *d*-spacing (16.5 Å, 15.6 Å and 14.8 Å) has been respectively achieved (Fig. 1a). We revealed an approximate linear dependence of the capacity dependence on interlayer spacing, and the maximum interlayer spacing (16.5 Å phase) results in a discharge capacity of 268.2 mA h g^{-1} at 0.1 A g^{-1} and an energy density of 328.5 W h kg^{-1}. More importantly, the PA intercalation also significantly increases the hydrophobility in the aqueous electrolyte, resulting in inhibition of the decomposition/dissolution of $VOPO_4{\cdot}2H_2O$ and remarkably improved cycling stability over 2000 cycles with a capacity retention of ~200 mA h g^{-1} at 5.0 A g^{-1}.

2. Results and discussion

2.1 Controllable PA intercalation

Uniform $VOPO_4{\cdot}2H_2O$ (JCPDS: 36-1472, labeled as VOP) nanoplates were first obtained by a conventional refluxing method reported previously.[11] After rapid solvothermal treatment of the as-prepared $VOPO_4{\cdot}2H_2O$ nanoplates in PA-containing isopropanol solvent at 60 °C for 2 h, the sharp (001) peak of pristine $VOPO_4{\cdot}2H_2O$ substantially shifted to a lower angle (5.3°) with much decreased intensity (Fig. 1b), corresponding to an extreme increase in basal spacing up to 16.5 Å with simultaneously reduced crystallinity during the intercalation. Fourier transform infrared spectroscopy (FTIR) reveals the presence of υ(N–H), υ(C–H), and δ(C–H) vibration modes and featured the peak of the benzene ring (Fig. 1c), demonstrating the successful intercalation of phenylamine molecules.[21,22] It is noteworthy that the characteristic peaks of crystal water in precursor $VOPO_4{\cdot}2H_2O$ completely disappear in the FTIR spectrum after PA-intercalation. Thermogravimetric analysis (TGA) (Fig. S1, ESI†) identifies a weight loss of 25.3% of PA–VOP up to 400 °C, corresponding to 0.6 units of the phenylamine molecule contained in one units of the PA–VOP structure. These results imply the phenylamine molecules replace the crystal water in the $VOPO_4{\cdot}2H_2O$ interlayer to well maintain the initial layered framework as follows:

$$VOPO_4{\cdot}2H_2O + 0.6PA \rightarrow PA_{0.6}@VOPO_4 + 2H_2O$$

Scanning electron microscope (SEM) observations show an edge-crimped plate like morphology with lateral size of 5 to 20 μm and increased thickness feature compared to the precursor VOP (Fig. 1d and Fig. S2, ESI†). However, transmission electron microscopy (TEM) and atomic force microscopy (AFM) characterization studies suggest a much smaller thickness of ~30 nm for our PA–VOP sample (Fig. S3, ESI† and Fig. 4). We consider that such a thickness difference should be caused by the possible liquid-exfoliation during the ultrasonic treatment of the sample preparation for TEM/AFM observation. In particular, one can clearly distinguish an interlayer spacing of ~1.6 nm from the cross-sectional high-resolution transmission electron microscope

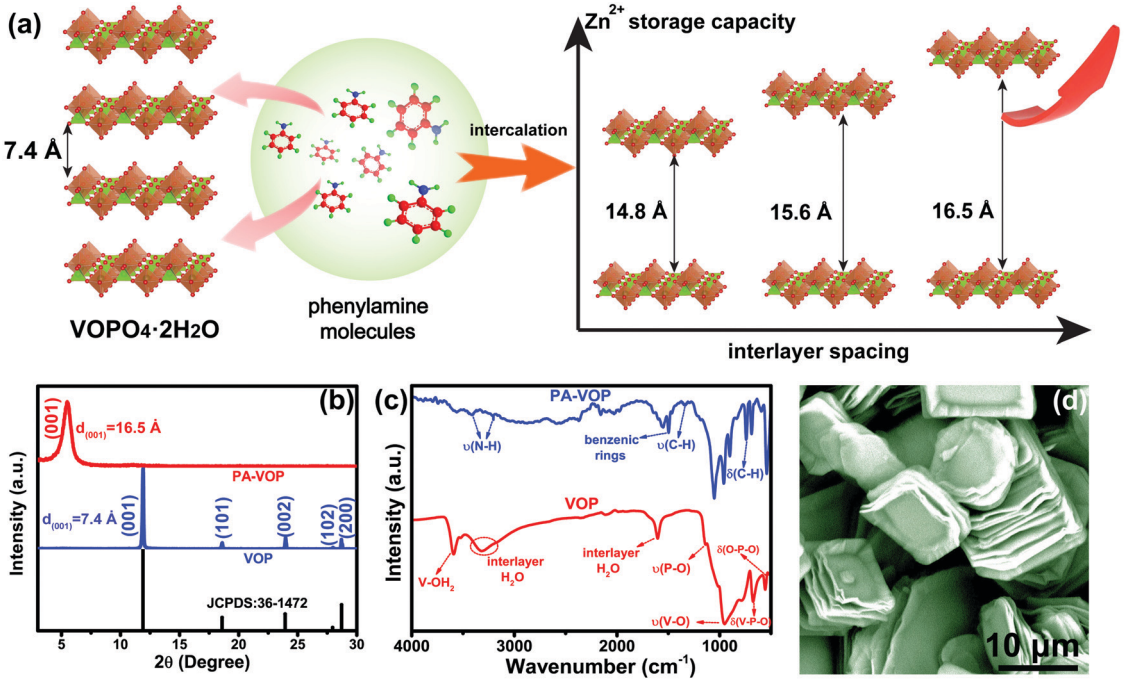

Fig. 1 (a) Scheme of capacity regulation for zinc-ion storage *via* PA-intercalation engineering. (b) Powder XRD patterns and (c) FTIR spectra of VOP and PA–VOP samples, respectively. (d) Typical SEM image of PA–VOP (16.5 Å phase).

(HRTEM) image (Fig. S4, ESI†), which is in good agreement with the one detected from the XRD data in Fig. 1b. Energy dispersive spectroscopy (EDS)-mapping profiles further clarify the uniform distribution of V, P, O, C, and N elements after PA intercalation (Fig. S4, ESI†).

2.2 Interlayer spacing dependence of Zn-ion storage

Interestingly, we found the interlayer spacing of the PA-intercalated samples can be carefully tuned by solvothermal treatment time. As shown in the XRD patterns in Fig. 2a and the enlarged patterns with a smaller angle range (4°–13°) in Fig. S5, ESI,† three PA–VOP samples with different interlayer spacing of 14.8, 15.6 and 16.5 Å can be obtained under a well-controlled solvothermal treatment time of 60, 90 and 120 min, respectively (Fig. 2a). A further increase of solvothermal treatment time compromises the interlayer spacing, indicating a saturated intercalation reaction at this threshold time (Fig. 2b). TGA curves suggest that the weight loss of PA–VOP (14.8 Å), PA–VOP (15.6 Å) and PA–VOP (16.5 Å) is 19.1%, 21.3% and 24.5% from 140 to 380 °C, respectively (Fig. S6, ESI†). Thus, it is rational that the increase of interlayer spacing is attributed to the higher content of intercalated phenylamine molecules upon prolonging the reaction time.[23] Note that the as-obtained interlayer spacing of 16.5 Å in our work is the maximal one among all of the reported layered cathodes for aqueous ZIBs such as layered δ-MnO_2, PA-MnO_2 and $Zn_{0.25}V_2O_5{\cdot}nH_2O$ (Fig. 2c).[7,12,24–30] SEM observation demonstrates the analogous plate-like morphology of the three PA–VOP samples other than a remarkably increased thickness caused by phenylamine insertion (Fig. 2d–f and Fig. 1d).

CR2032 coin cells were then assembled employing these PA–VOP samples as the cathode material (slurry mass loading: ~2 mg cm^2), Zn foil as the anode and 2 M $Zn(CF_3SO_3)_2$ solution as the aqueous electrolyte, respectively. Typical cyclic voltammetry (CV) curves of the Zn//PA–VOP (16.5 Å phase) battery reveals a general active process in the first scan cycle, while the curves of the stabilized second and third cycle give a pair of oxidation/reduction peaks located at around 1.6 V and 1.3 V, respectively (Fig. S6, ESI†). It is noteworthy that PA molecules are generally inactive in mild aqueous electrolyte, and the electrochemical activity and capacity contribution should be mostly provided from the $VOPO_4$ framework.[31–33] The galvanostatic charge discharge (GCD) curves also exhibit steady charge and discharge plateaus with good agreement with the voltage range in CV curves (Fig. S7 and S8, ESI†). It has been reported that the non-metal protons (H^+) have also been recognized as charge carrier ions for some aqueous batteries.[34] To clarify this, we compare the electrochemical performance on both aqueous and non-aqueous systems (0.5 M $ZnSO_4$/acetonitrile, Fig. S9, ESI†). No apparent difference has been observed between the CV peaks, thereby ruling out the possible contribution from proton intercalation in our system. *Ex situ* XRD at different voltages in the second cycle reveals a reversible Zn^{2+} intercalation/de-intercalation mechanism of the PA–VOP cathode (Fig. S10, ESI†).

We found the specific capacity of the PA–VOP cathodes is quite dependent on its interlayer spacing. As shown in Fig. 2g, the pristine VOP (7.4 Å) and the PA–VOP samples (14.8 Å phase, 15.6 Å phase and 16.5 Å phase) deliver a discharge capacity of 138.4 mA g^{-1}, 226.5 mA h g^{-1}, 243.7 mA h g^{-1}, and 268.2 mA h g^{-1}, respectively. Similar enhancement tendency has been also observed for rate-capacity of series of layered phosphates as

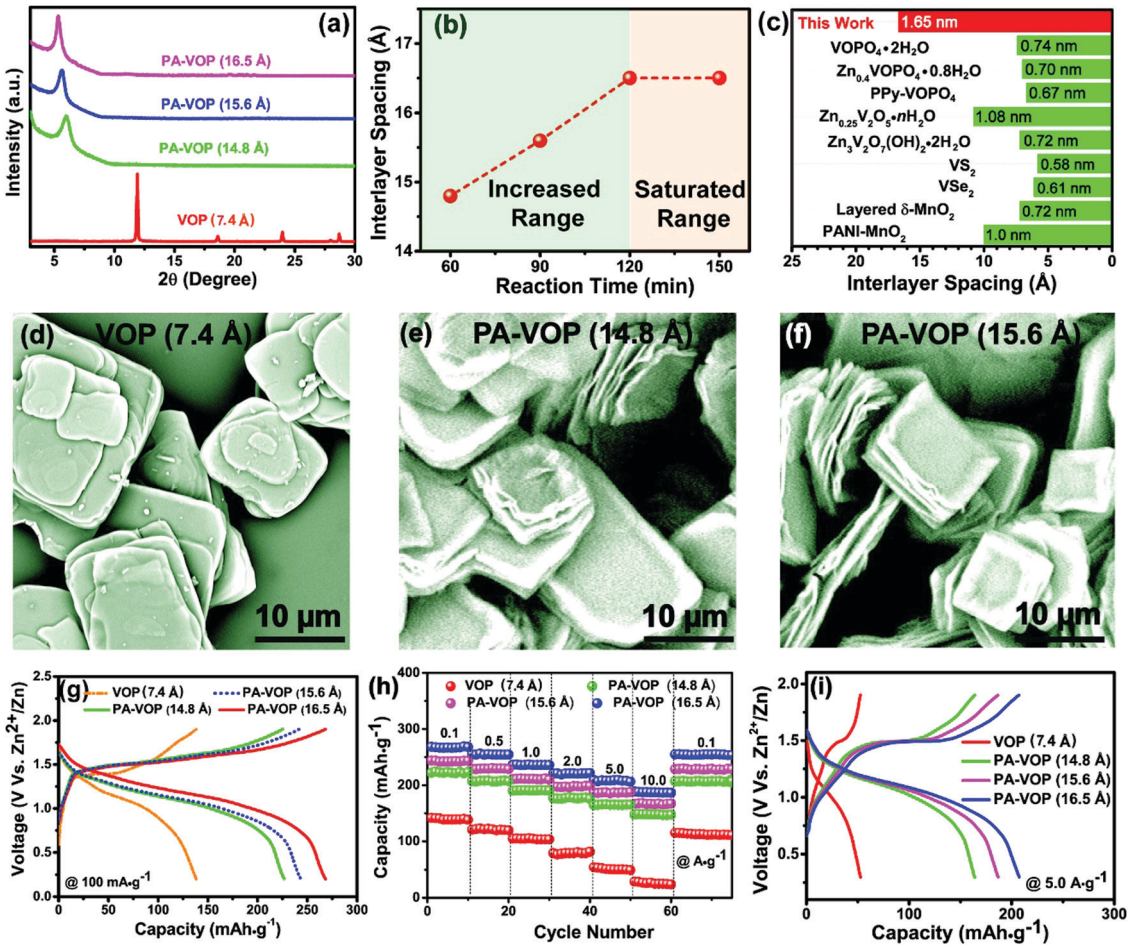

Fig. 2 (a) XRD patterns of various PA–VOP samples synthesized under different temperatures and solvents. (b) Dependence of interlayer spacing and solvothermal time. (c) Typical layered materials served as the cathode of aqueous ZIBs.[7,12,24–30] (d–f) SEM image of VOP, PA–VOP (14.8 Å phase) and PA–VOP (15.6 Å phase) samples, respectively. (g) GCD curves of VOP based ZIB and PA–VOP based ZIBs with adjustable interlayer spacing, respectively (14.8, 15.6 and 16.5 Å). (h) Cycle tests at a varied current density of VOP and PA–VOP cathodes with different interlayer spacing, respectively. (i) GCD curves of VOP and PA–VOP cathode with different interlayer spacing at a current density of 5 A g^{-1}, respectively.

shown in Fig. 2h. The resultant 16.5 Å phase delivers the maximum rate capability (Fig. 2i): high specific capacities of 268.2, 254.8, 236.4, 220.7, 207.2, and 187.5 mA h g^{-1} have been respectively realized at current densities of 0.1, 0.5, 1.0, 2.0, 5.0, and 10.0 A g^{-1} with a recovered capacity of 253.3 mA h g^{-1} when the applied current density turned back to 0.1 A g^{-1}. To figure out the impact on electrochemical performance of the PA–VOP cathode contributed by the PA molecule itself,[35] we further performed a contrast test by employing pure PA as the cathode, Zn foil as the anode and 2 M $Zn(CF_3SO_3)_2$ as the electrolyte, respectively. CV curves at different scan rates display similar capacitive-like results in the voltage range of 0.2 to 1.9 V, while the corresponding GCD curves give a slight specific capacity of 13.3, 12.1 10.8, 8.6, and 7.9 mA h g^{-1} of the PA cathode at the current density of 0.1, 0.2, 0.5, 1.0, and 2.0 A g^{-1}, respectively (Fig. S11, ESI†). In contrast, our 16.5 Å phase PA–VOP cathode exhibits a capacity of 268.2 mA h g^{-1} at 0.1 A g^{-1}, which is remarkably higher than that of the pure PA or VOP sample. This result suggests some possible chelation effect on Zn storage in our PA–VOP composites.[35] In fact, considering the various valence changes of V in the $VOPO_4$ framework during the electrochemical reaction, the theoretical specific capacity of layered $VOPO_4{\cdot}2H_2O$ should be higher than 300 mA h g^{-1}.[36] Limited by the sluggish diffusion of Zn^{2+} and strong electrostatic interactions between Zn^{2+} and the $VOPO_4{\cdot}2H_2O$ host,[9] the real specific capacity of layered $VOPO_4{\cdot}2H_2O$ is only 138.4 mA g^{-1} in our work. Such a sluggish diffusion issue of Zn^{2+} has been well addressed after the controllable intercalation of PA in the interlayer, which has been confirmed by GITT characterization and also DFT calculation as discussed below. Accordingly, we can realize a much-enhanced capacity (268.2 mA h g^{-1}) which is close to the theoretical specific capacity of layered $VOPO_4{\cdot}2H_2O$.

We reveal that the capacity–interlayer spacing dependence could follow an approximate linear trend with a slope of ~14.3 as summarized in Fig. 3a. The specific capacity of the 16.5 Å phase (268.2 mA h g^{-1}) at a current density of 0.1 A g^{-1} is about two times higher than that of pristine VOP (138.4 mA h g^{-1}) and also well above that of the layered PPy–$VOPO_4$ cathode (~80 mA h g^{-1}) reported before.[25] Meanwhile, one can see a voltage plateau *versus*

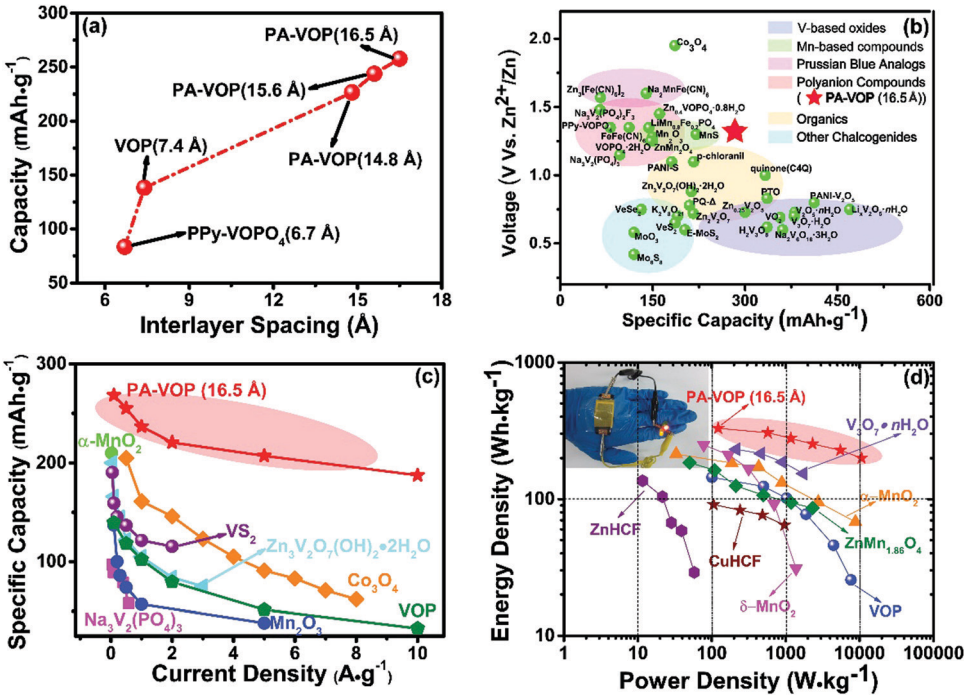

Fig. 3 (a) Dependence of specific capacity and interlayer spacing of various $VOPO_4$-based cathodes at the current density of 0.1 A g^{-1}.[23] (b) Voltage plateau *versus* specific capacity for various mainstream cathodes recently reported and our PA–VOP (16.5 Å) cathode.[5–7,17,24–28,37–57] (c) Comparison of the rate-capacity between our PA–VOP cathode and the other recently reported cathodes for aqueous ZIBs.[27,44,50,57,58] (d) Ragone plot of the PA–VOP cathode and a series of other cathode materials reported previously.[29,39,45,48,59,60] Inset is a solid-state battery constructed from the PA–VOP@CFC cathode driving a group of LEDs.

specific capacity diagram for mainstream cathodes of aqueous ZIBs reported in recent years (V-based oxides,[5,17,26,27,37–43] Mn-based compounds,[44–46] Prussian Blue analogs,[47–49] polyanion compounds,[7,24,25,50–52] organics[31,53–56] and other chalcogenides[6,28,30,57]) shown in Fig. 3b. Benefitting from the *d*-spacing dependent performance as shown above, it is evident that the rate-capacity of our optimal PA–VOP sample (16.5 Å phase) surpasses most traditional materials including Mn-based oxides (α-MnO_2,[58] Mn_2O_3,[44]), V-based compounds ($Na_3V_2(PO_4)_3$,[50] $Zn_3V_2O_7(OH)_2{\cdot}2H_2O$[27]) and Co_3O_4[57] reported recently (Fig. 3c). Taking advantage of its high specific capacity of 268.2 mA g^{-1} and prominent discharge plateau (~1.3 V), the 16.5 Å-phase PA–VOP renders a high energy density of 328.5 W h kg^{-1} at a power density of 122.6 W kg^{-1}, having apparent advantages in contrast with various popular cathode materials such as $V_3O_7{\cdot}nH_2O$,[39] α-MnO_2,[59] δ-MnO_2,[29] $ZnMn_{1.86}O_4$,[45] ZnHCF[47] and CuHCF[60] (Fig. 3d). These excellent energy and power densities promote the application in flexible and wearable electronic devices (inset in Fig. 3d).

2.3 Reaction/diffusion kinetics mechanism

In order to clarify the aforementioned *d*-spacing dependent battery-performance, a corresponding study on electronic conductivity and zinc-ion diffusion kinetics is further conducted. A four-probe conductivity test shows a 2–7 times higher electronic conductivity of PA–VOP (16.5 Å) in contrast to that of pristine VOP with increased pressure, which is mainly attributed to the intrinsic high conductivity of phenylamine (Fig. 4a). When carefully analyzing the dependence between specific capacity and electronic conductivity, interestingly, we can also obtain an approximate linear tendency that is highly analogous to the linear tendency between the specific capacity and *d*-spacing (Fig. S12, ESI†). It is generally believed that high electronic conductivity of the electrode materials is favorable for a superior specific capacity for battery application.[61] Thus, it is rational that the "approximate linear tendency" between the *d*-spacing of PA–VOP and its specific capacity should originate from the linear increase of the electronic conductivity. CV curves at varied scan rates are employed to distinguish the capacitive/ion diffusion contribution by analyzing the dependence of the logarithm of peak current density and the scan rate (Fig. S13, ESI†). Theoretically, the peak current (i) and sweep rate (v) in the CV curve follows the rule:[62,63]

$$i = av^b \quad (1)$$

where a and b are adjustable values. A b value of 0.5 indicates a semi-infinite diffusion mechanism, while a b value of 1.0 suggests capacitive behavior. In our case, the b value for the predominant peaks of a VOP, PA–VOP (14.8 Å phase) and PA–VOP (16.5 Å phase) cathode is determined to be 0.63, 0.73 and 0.76, respectively (Fig. S13, ESI†). Apparently, the capacitive contribution in the PA–VOP (16.5 Å phase) cathode is 44.8%, 49.6%, 56.7%, 60.4%, and 65.9% at a scan rate of 0.1, 0.2, 0.5, 0.8, and 1.0 mV s^{-1}, respectively. These values are much higher than those in the VOP cathode (28.4%, 33.2%, 38.9%, 42.8%,

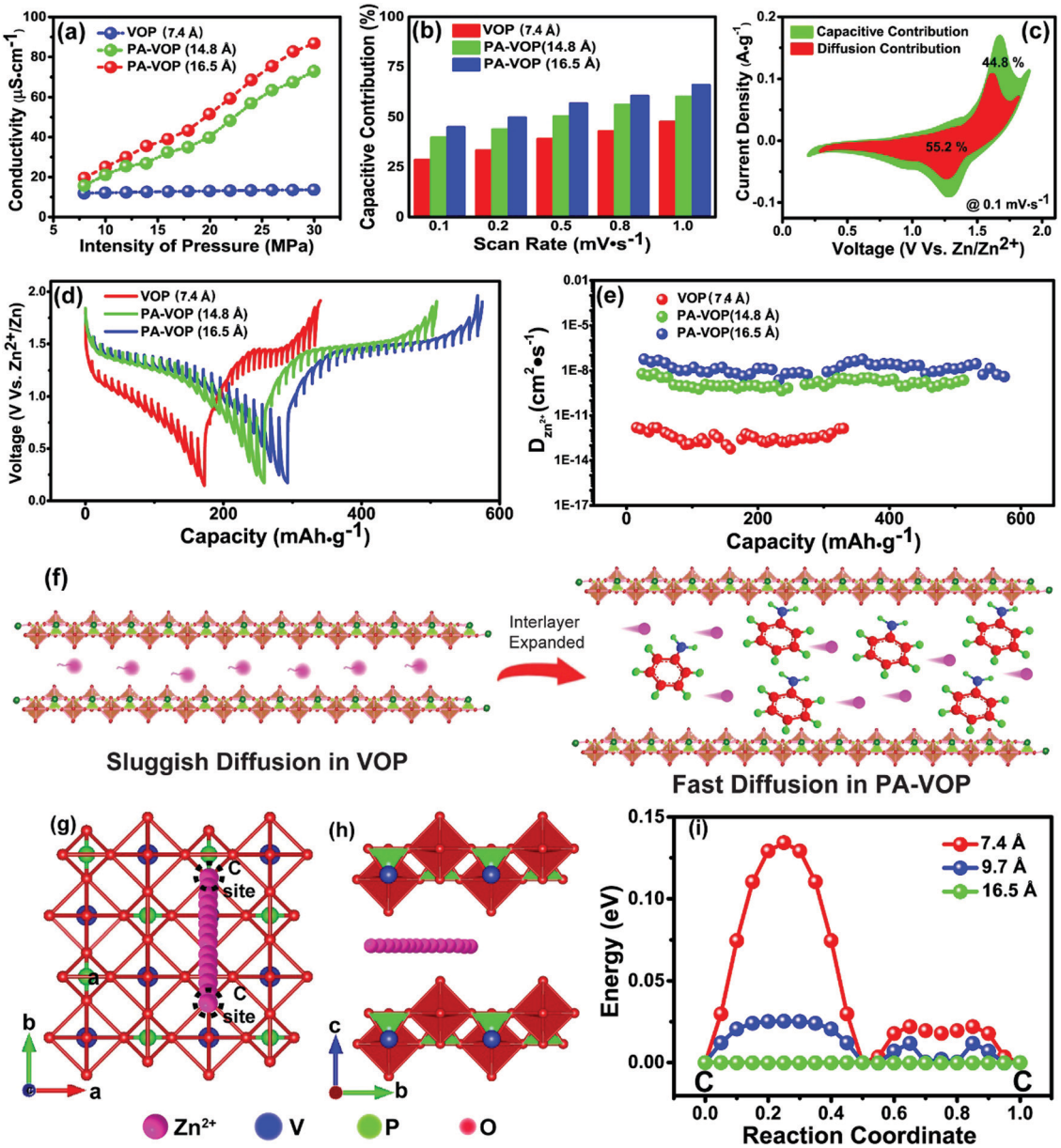

Fig. 4 (a) Electronic conductivity test under different pressure. (b) Capacitive contribution of VOP, PA–VOP (14.8 Å phase) and PA–VOP (16.5 Å phase), respectively. (c) CV curve containing the schematic of the capacitive and diffusion contribution of the PA–VOP (16.5 Å phase) cathode at the scan rate of 0.1 mV s^{-1}. (d) GITT curve and (e) the calculated diffusion coefficient of VOP, PA–VOP (14.8 Å phase) and PA–VOP (16.5 Å phase), respectively. (f) Schematic illustration of Zn^{2+} diffusion kinetics in PA–VOP and VOP cathode. (g) Zinc-ion diffusion path scheme in the top view and (h) side view mode. (i) Calculated energy barrier curve of the PA–VOP samples with different interlayer spacing.

and 47.5% at 0.1, 0.2, 0.5, 0.8, and 1.0 mV s^{-1}, respectively) (Fig. 4b and c).

On the other hand, zinc-ion diffusion kinetics is further identified by a galvanostatic intermittent titration technique (GITT) (Fig. 4d). Strikingly, an ultrahigh zinc-ion diffusion coefficient of $\sim 5.7 \times 10^{-8}$ cm^{-2} s^{-1} has been detected in the 16.5 Å phase, nearly 5 orders of magnitude higher than that of the pristine VOP cathode (6.2×10^{-13} cm^{-2} s^{-1}) and also much higher than that of conventional cathode materials reported recently including V_2O_5, $ZnMn_2O_4$, $Zn_3V_2O_7(OH)_2{\cdot}2H_2O$, and $K_2V_8O_2$[27,41,45,64] (Fig. 4e). This drastic increase demonstrates a great improvement in terms of Zn^{2+} intercalation/de-intercalation kinetics by an enlarged 2D interlayer channel as illustrated in Fig. 4f. In principle, a large zinc-ion diffusion coefficient is generally observed in ultrathin samples due to the shortened effective diffusion path and larger activated surface, which drastically facilitate Zn^{2+} diffusion and charge transfer.[30,65,66] Our previous study also confirms a fast Zn-ion diffusion ability in 6.0 nanometer ultrafine spinel oxide nanodots.[66] However, in the present study, the as-obtained 16.5 Å phase shows a significant increase in thickness compared with the pristine VOP sample (Fig. 2d–f). Therefore, the thick samples display

much faster kinetics than that of thin VOP samples unusually.[65,67] Such a phenomenon suggests that the zinc-ion transport in our layered phosphate series is dominated by interlayer diffusion on account of the fact that an enlarged interlayer spacing would provide high-efficiency 2D ion diffusion/hopping channels.

Besides, density functional theory (DFT) based first-principles simulation is conducted for a deeper understanding of the greatly improved diffusion kinetics. A climbing-image nudged elastic band (CI-NEB) method is adopted to reveal the possible diffusion paths and the corresponding energy barrier of zinc ions. The interlayer site on the top of the corner-shared oxygen atom of the [PO_4] tetrahedron and [VO_6] octahedron gives an optimal absorption energy of 0.07 eV, which can be determined as the potential adsorption site (called the C site) for zinc-ion diffusion. The as-optimized diffusion path denotes a hopping process through the right above site of the [VO_6] octahedron and [PO_4] tetrahedron between the adjacent C sites (Fig. 4g and h). Subsequently, an interlayer-dependent activation energy decrease tendency is derived based on such a diffusion path. The energy barrier for zinc-ion diffusion in VOP bulk (7.4 Å) is calculated to be 0.13 eV, and dramatically decreases to a much lower value ($\sim$0.03 eV) until a threshold interlayer spacing of 9.7 Å. A further increase in the spacing gives rise to a slight change in the energy barrier, and it finally decreases to $\sim 2.3 \times 10^{-4}$ eV for the PA–VOP (16.5 Å phase) sample.

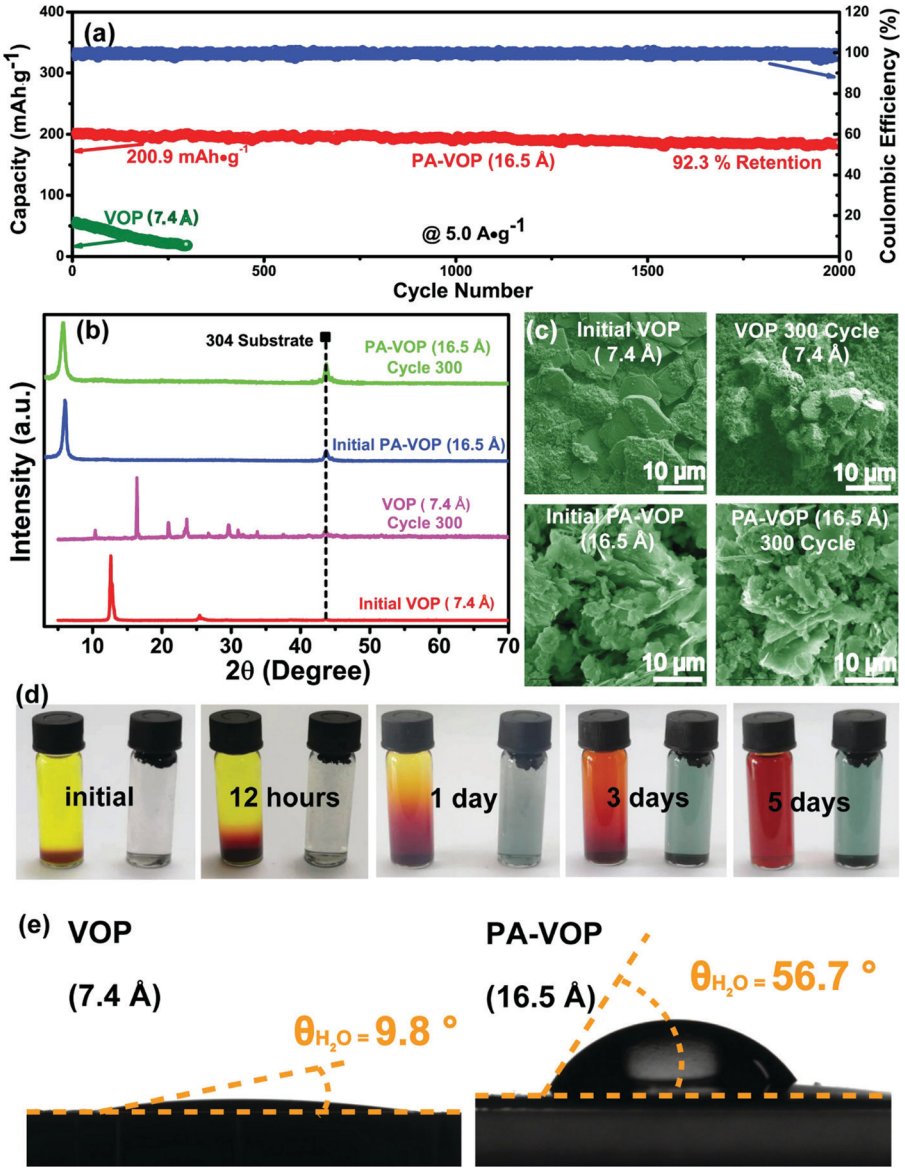

Fig. 5 (a) Long-term cycle test of Zn//VOP and Zn//PA–VOP (16.5 Å phase) batteries using 2 M $Zn(CF_3SO_3)_2$ aqueous electrolyte. (b) XRD patterns and (c) SEM images of the VOP and PA–VOP (16.5 Å phase) cathode before and after 300 cycles, respectively. (d) Optical photographs of the as-dispersed VOP and PA–VOP (16.5 Å phase) powder in 2 M $ZnSO_4$ aqueous electrolyte at different times. (e) Water-based angle contact experiment of VOP and PA–VOP (16.5 Å phase) powder.

Consequently, the greatly enhanced diffusion kinetics, predominant capacitive contribution and high electronic conductivity in PA–VOP samples provide the essential insight for the interlayer spacing dependent Zn^{2+} storage performance.

2.4 Cyclability improvement

It is known that a layered $VOPO_4{\cdot}nH_2O$ cathode undergoes severe capacity/voltage fading with rather poor cyclability originating from the decomposition/dissolution of $VOPO_4{\cdot}nH_2O$ in mild aqueous electrolyte.[9] Interestingly, we found that the chemical stability and electrochemical reversibility was significantly enhanced after the PA intercalation. Compared to aqueous $Zn(SO_4)_2$ electrolyte, a superior lifespan was observed in the $Zn(CF_3SO_3)_2$ electrolyte due to the better desolvation effect of bulky $(CF_3SO_3)^-$ *versus* $(SO_4)^{2-}$ (Fig. S14, ESI†). One can see the Zn//2 M $Zn(CF_3SO_3)_2$//PA–VOP (16.5 Å phase) battery delivers an initial specific capacity of 200.9 mA h g^{-1} and a steady cycle stability of 92.3% capacity retention after 2000 cycles under a high current density of 5.0 A g^{-1}. In contrast, the VOP based battery just exhibits an inferior capacity of ~60 mA h g^{-1} with rapid decay in the first 300 cycles (Fig. 5a). To clarify the actual mechanism, *ex situ* XRD characterizations of the VOP and PA–VOP (16.5 Å phase) cathode before and after 300 cycles are carried out as shown in Fig. 5b. Apparently, the characteristic diffraction peaks of the VOP cathode completely disappear after 300 cycles, indicating the phase conversion of VOP during the long-term cycling. In contrast, the PA–VOP (16.5 Å phase) cathode well maintained the initial phase without any impurity diffraction peaks. SEM observation also reveals that the PA–VOP (16.5 Å phase) sample well maintains the initial plate-like morphology compared to the drastic aggregation of the VOP cathode after 300 cycles (Fig. 5c). All results demonstrate the greatly enhanced structural reversibility of our PA–VOP sample after PA intercalation.

To further probe the origin of the remarkable difference in long-lifespan, we compare the chemical stability of both VOP and PA–VOP samples in aqueous 2 M $ZnSO_4$ electrolyte. As shown in Fig. 5d, it is clear that the VOP sample generally disappears in the bottom of the solution followed by a typical color change to deep red after 5 days due to the decomposition/dissolution of $VOPO_4{\cdot}nH_2O$ into VO_x(s) and PO_4^{3-}.[9] However, the PA–VOP (16.5 Å phase) sample still floats on the liquid surface with much better stability after 5 days (Fig. 5d). Such a result inspires our consideration of the difference in surface-wettability of these two samples. Accordingly, Fig. 5e compares the water-based contact angle on the surface of a pressed powder of the VOP and PA–VOP sample. The PA–VOP and VOP sample shows a contact angle of 56.7° and 9.8° respectively, demonstrating the surface is much more hydrophobic after PA intercalation. Rationally, this hydrophobic surface plays a decisive role in inhibiting the decomposition/dissolution of $VOPO_4$ in aqueous electrolyte, thus leading to a much improved long lifespan of the as-constructed ZIBs. Most recently, Sun *et al.* reported that the decomposition/dissolution of $VOPO_4{\cdot}2H_2O$ can be prevented by PO_4^{3-} addition and high salt concentration of the aqueous electrolyte.[9] Such a strategy promotes long-term cycling over 500 cycles with a stable capacity of only 90 mA h g^{-1} at 2.0 A g^{-1} but also increases the battery cost. In contrast, our strategy by PA-intercalation requires no addition of any reagent/salt addition, and realizes much superior cycling stability over 2000 cycles with a capacity of ~200 mA h g^{-1}.

Note that the influence of electrode hydrophobicity on cell performance could be comprehensive. To reveal the Zn-ion diffusion inside PA–VOP and also Zn-ion transfer at the PA–VOP/electrolyte interface, an electrochemical impendence spectrum study is carried out and the corresponding Nyquist plot is shown in Fig. S15, ESI.† It can be seen that the plots of the pure VOP (7.4 Å) cathode after a specific cycle (1st cycle and 10th cycle) consist of an intercept on the real part axis, one semicircle in the high-frequency region and a straight line in the low-frequency region, corresponding to a series resistance of 5.3 Ω, a charge transfer resistance of 215.4 Ω, and a Warburg diffusion impendence of 237.6 Ω, respectively. However, for the PA–VOP (16.5 Å) composited cathode, the corresponding values have been determined to be 1.2 Ω, 57.8 Ω and 82.3 Ω, respectively, which is significantly lower than that of the VOP (7.4 Å) cathode. More importantly, the PA–VOP (16.5 Å) composited cathode delivers a smaller semicircle between the region of series resistance and charge transfer resistance, which should be attributed to the electrolyte/electrode interface resistance (23.2 Ω) caused by the enhanced hydrophobicity.[68,69] No apparent changes were observed for both the pure VOP (7.4 Å) and PA–VOP (16.5 Å) composited cathode after 10 electrochemical cycles. According to these results, it is rational that the PA–VOP sample with enhanced hydrophobicity actually results in two influencing effects on the Zn ion diffusion: firstly, a significantly reduced diffusion and charge transfer impendence which is favorable for the Zn ion diffusion inside the PA–VOP layer. Secondly, Zn-ion transfer at the PA–VOP/electrolyte interface is more difficult as evident by the appearance of electrolyte/electrode interface resistance. The former should be dominant in our present work because remarkably improved capacity and cyclability has been detected in the PA–VOP sample.

3. Conclusions

In summary, we developed a controllable phenylamine-intercalation strategy for layered vanadium phosphates with various interlayer spacings (14.8 Å, 15.6 Å and 16.5 Å). The crystal water in $VOPO_4{\cdot}2H_2O$ was extracted from the interlayer space accompanied by the PA intercalation. The specific capacity is quite dependent on the *d*-spacing in the PA–VOP system followed by an approximate linear tendency, and the interlayer spacing (16.5 Å) results in a maximum capacity of 268.2 mA h g^{-1} at 0.1 A g^{-1} and an energy density of 328.5 W h kg^{-1}. Both of the experimental data and theoretical calculation identify that the enlarged spacing can boost fast zinc-ion diffusion with an ultrahigh diffusion coefficient of $\sim 5.7 \times 10^{-8}$ cm^{-2} s^{-1}. The intercalation of PA molecules also significantly increases the hydrophobicity in the aqueous electrolyte, inhibiting the decomposition/dissolution of $VOPO_4{\cdot}$

$2H_2O$ and remarkably improving the long-term cycling stability over 2000 cycles at 5.0 A g^{-1} with a capacity of ~200 mA h g^{-1}. Our study develops a feasible solution for the sluggish Zn^{2+} diffusion kinetics and poor stability of layered $VOPO_4{\cdot}2H_2O$, and also provides clear guidance on the interlayer chemistry principle toward high-performance zinc-ion batteries.

4. Experimental section

4.1 Materials synthesis

The $VOPO_4{\cdot}2H_2O$ sample was synthesized based on a reported refluxing method with some modifications. Typically, 4.8 g V_2O_5, 26.6 mL H_3PO_4 and 115.4 mL DI water is added to a three-necked flask, respectively, followed by 30 min of magnetic stirring with the addition of 10 mL of HNO_3 to stabilize the oxidation state of vanadium.[70] The mixture is then heated at 110 °C for 16 h. Yellow precipitate is collected from the bottom after cooling down to room temperature, the yellow precipitate is collected by centrifugation, and washed with DI water and acetone 3 times, respectively. The resulting bright yellow VOP sample was dried at 60 °C in a vacuum oven. To introduce phenylamine molecules into the interlayer spacing of VOP, 0.3 g of as-synthesized VOP is mixed with 30 mL of isopropanol in a 50 mL Teflon-lined strain-less steel autoclave followed by the addition of 5 mL phenylamine. The mixture is stirred for 15 min and then heated in an oven at 60 °C for a short time (60, 90 and 120 min) to obtain phenylamine intercalated $VOPO_4$ (PA–VOP) with varied interlayer spacing (14.8, 15.6 and 16.5 Å), respectively. The black brown sediment on the bottom is then collected and washed with ethanol 3 times. The PA–VOP powder is finally obtained after vacuum drying at 60 °C for 6 h.

4.2 Materials characterization

The structure morphology and structure characterization are characterized by scanning electron microscopy (SEM, Phenom Pro X), transmission electron microscopy (TEM, Philips CM 200 FEG Field Emission Microscope) and X-ray diffraction (XRD, Bruker D8-A25 diffractometer using Cu Kα radiation (λ = 1.5406 Å)). Atomic force microscopy (AFM) images are acquired in tapping mode by depositing the nanosheets on Si wafers (SPM 9700). The high resolution transmission electron microscopy (HRTEM) and energy dispersive spectroscopy mapping (EDS-mapping) are carried along with TEM measurements to gather detailed information on the phase structure and chemical element distribution of the sample, respectively. Further information on the chemical bonding and microscopic conditions is revealed by means of Fourier transform infrared spectroscopy (FTIR, BRUKER TENSOR II) and thermogravimetric analysis (TGA, SDT Q600), respectively. A water-based angle contact experiment (JY-82) was developed based on the pressed powder of PA–VOP and VOP samples. Electronic conductivity tests were carried out on a four-probe conductivity tester (ST2253y).

4.3 Electrochemical measurement

PA–VOP and VOP based cathodes of aqueous ZIBs are respectively fabricated by mixing as-prepared samples, acetylene black and polyvinylidene fluoride (PVDF) on the basis of a mass ratio of 7 : 2 : 1 with the addition of 1-methyl-2-pyrrolidinone (NMP), then the uniform slurry is coated onto a piece of 304 stainless steel foil and dried at 100 °C for 12 h in a vacuum oven. The slurry-coated foil is cut into a Φ 15 mm electrode as the cathode, while the zinc foil washed with ethanol and glass fiber membrane is used as the anode and separator, respectively, and 2 M $Zn(CF_3SO_3)_2$ is prepared as the electrolyte. The CR-2032 cell was assembled in air using the previous electrodes and other relevant components. A LAND battery test system (CT2001A) was employed to evaluate the electrochemical performance of the battery: galvanostatic charge–discharge (GCD), rate capability and long-term cycle performance. Cyclic voltammetry (CV) tests at different scan rates and an electrochemical impedance spectrum (EIS) with a frequency range from 100 kHz to 0.01 Hz together with an applied AC of 5 mV is performed on an electrochemical workstation (CHI660E), respectively. A galvanostatic intermittent titration technique (GITT) is performed under a modified GCD mode, in which an operation period includes two parts: a charge/discharge procedure lasting for 10 min at 0.05 A g^{-1} and a subsequent pause time for 10 min.

4.4 Fabrication of the flexible quasi-solid-state battery

The quasi solid flexible zinc-ion battery was fabricated using the aforementioned slurry-coated carbon fiber cloth (CFC) as the cathode (mass loading: 2 mg cm^{-2}), CFC with a layer of zinc electrodeposited coating as the anode, a piece of filter paper as the separator and 2 M $Zn(ClO_4)_2$@polyvinyl alcohol (PVA) (aqueous) as the electrolyte. $Zn(ClO_4)_2$ is chosen here for its better solubility in PVA solution compared to $ZnSO_4$ and $Zn(CF_3SO_3)_2$.[24] The electrolyte was prepared by adding 3 g PVA to 30 mL 2 M $Zn(ClO_4)_2$ aqueous solution little by little with continuous stirring, followed by oil bath treatment at 80 °C for 2 h and gathering the thick sample when it came to room temperature. The electrochemical deposition of a zinc layer on the CFC was executed on CHI660E using a potentiostatic mode at −0.7 V (*vs.* Zn^{2+}/Zn) for 2000 s. The ultimate flexible quasi-solid-state battery was assembled and sealed with polyimide (PI) film to form a stable sandwich structure.

4.5 Electrochemical calculation method

The calculation method for the capacity contribution of the cathodes is based on the following equation:

$$I_p = C_1 v + C_2 v^{\frac{1}{2}} \quad (2)$$

where I_p (A g^{-1}) is the peak current density at different scan rates, v (mV s^{-1}) is the specific scan rate, and C_1 and C_2 are the corresponding constant factors of the capacity contribution of the surface pseudocapacitive effect and battery-type effect, respectively.

With a deformation of the above equation, the specific contribution rate of different internal mechanisms can be

solved according to the following equation:

$$\frac{I_p}{v^{\frac{1}{2}}} = C_1 v^{\frac{1}{2}} + C_2 \quad (3)$$

The specific energy density (W h kg^{-1}) and average specific power density (W kg^{-1}) of the batteries is calculated in terms of the following equations:

$$E_s = \int_{V_0}^{V_1} C_s(V) \quad (4)$$

$$P_s = \frac{E_s}{t} \quad (5)$$

where E_s is the calculated specific energy density (W h kg^{-1}), P_s is the average specific power density (W kg^{-1}); C_s (mA h g^{-1}) is the specific capacity of the battery, V_0 and V_1 are the voltage lower limit and voltage upper limit of the discharge procedure, respectively, and t is the discharge time (h). All the parameters calculated are based on the mass loading of the active materials (VOP or PA–VOP).

The diffusion coefficient ($D_{Zn^{2+}}$) of zinc ions can be experimentally calculated by a GITT method in terms of the following equation:[17]

$$D = \frac{4}{\pi\tau} L^2 \left(\frac{\Delta E_s}{\Delta E_t}\right)^2 \quad (6)$$

where D is the diffusion coefficient of zinc ions, τ is the relaxation time of the current pulse, L is the diffusion length which is approximate to the thickness of coated slurry, and ΔE_s and ΔE_t are the voltage changes produced by the current pulse and the galvanostatic charge/discharge, respectively.

4.6 Simulation details

The modeling in this study was performed in the framework of the DFT as implemented in the Vienna Ab initio Simulation Package (VASP). The functional of Perdew–Burke–Ernzerhof based on the generalized gradient approximation (GGA) was applied to describe the exchange–correlation energy. In addition, the zero damping DFT-D3 dispersion correction method of Grimme accounted for VdW interaction in the system. A vacuum space of 15 Å was adopted. The plane-wave cutoff energy was set to be 480 eV, and the k-mesh was determined to be $7 \times 7 \times 1$ according to the convergence test, which makes the energy accuracy within 1.0×10^{-3} eV per atom. Finally, a double-layered $VOPO_4$ model was constructed, with the corresponding interlayer spacing obtained from our previous XRD and HRTEM analysis, thereby the diffusion of zinc ions between $VOPO_4$ layers was simulated using the climbing-image nudged elastic band method.

Conflicts of interest

The authors declare no conflict of interest.

Acknowledgements

This work was financially supported by the National Natural Science Foundation of China (No. 51872051 and 51731004), the Science and Technology Committee of Shanghai Municipality (18520723100), and the Fundamental Research Funds for the Central Universities (2242021R10119).

References

1 J. W. Choi and D. Aurbach, *Nat. Rev. Mater.*, 2016, **1**, 16013.
2 P. Canepa, G. S. Gautam, D. C. Hannah, R. Malik, M. Liu, K. G. Gallagher, K. A. Persson and G. Ceder, *Chem. Rev.*, 2017, **117**, 4287–4341.
3 G. Z. Fang, J. Zhou, A. Q. Pan and S. Q. Liang, *ACS Energy Lett.*, 2018, **3**, 2480–2501.
4 A. Konarov, N. Voronina, J. H. Jo, Z. Bakenov, Y. K. Sun and S. T. Myung, *ACS Energy Lett.*, 2018, **3**, 2620–2640.
5 Q. Pang, C. L. Sun, Y. H. Yu, K. N. Zhao, Z. Y. Zhang, P. M. Voyles, G. Chen, Y. J. Wei and X. D. Wang, *Adv. Energy Mater.*, 2018, **8**, 1800144.
6 H. F. Li, Q. Yang, F. N. Mo, G. J. Liang, Z. X. Liu, Z. J. Tang, L. T. Ma, J. Liu, Z. C. Shi and C. Y. Zhi, *Energy Storage Mater.*, 2019, **19**, 94–101.
7 F. Wang, W. Sun, Z. Shadike, E. Y. Hu, X. Ji, T. Gao, X. Q. Yang, K. Xu and C. S. Wang, *Angew. Chem., Int. Ed.*, 2018, **57**, 11978–11981.
8 F. Wan, Y. Zhang, L. L. Zhang, D. B. Liu, C. D. Wang, L. Song, Z. Q. Niu and J. Chen, *Angew. Chem., Int. Ed.*, 2019, **58**, 7062–7067.
9 H. Y. Shi, Y. Song, Z. M. Qin, C. C. Li, D. Guo, X. X. Liu and X. Q. Sun, *Angew. Chem., Int. Ed.*, 2019, **58**, 16057–16061.
10 Z. Y. Wu, L. Jiang, W. C. Tian, Y. A. Wang, Y. C. Jiang, Q. F. Gu and L. F. Hu, *Adv. Energy Mater.*, 2019, **9**, 1900111.
11 C. Z. Wu, X. L. Lu, L. L. Peng, K. Xu, X. Peng, J. L. Huang, G. H. Yu and Y. Xie, *Nat. Commun.*, 2013, **4**, 2431.
12 J. H. Huang, Z. Wang, M. Y. Hou, X. L. Dong, Y. Liu, Y. G. Wang and Y. Y. Xia, *Nat. Commun.*, 2018, **9**, 2906.
13 M. H. Han, E. Gonzalo, G. Singh and T. Rojo, *Energy Environ. Sci.*, 2015, **8**, 81–102.
14 G. Wang, J. Zhang, S. Yang, F. X. Wang, X. D. Zhuang, K. Mullen and X. L. Feng, *Adv. Energy Mater.*, 2018, **8**, 1702254.
15 M. L. Mao, T. Gao, S. Y. Hou and C. S. Wang, *Chem. Soc. Rev.*, 2018, **47**, 8804–8841.
16 X. Ji, J. Chen, F. Wang, W. Sun, Y. J. Ruan, L. Miao, J. J. Jiang and C. S. Wang, *Nano Lett.*, 2018, **18**, 6441–6448.
17 Y. Q. Yang, Y. Tang, G. Z. Fang, L. T. Shan, J. S. Guo, W. Y. Zhang, C. Wang, L. B. Wang, J. Zhou and S. Q. Liang, *Energy Environ. Sci.*, 2018, **11**, 3157–3162.
18 L. M. Zhou, Q. Liu, Z. H. Zhang, K. Zhang, F. Y. Xiong, S. S. Tan, Q. Y. An, Y. M. Kang, Z. Zhou and L. Q. Mai, *Adv. Mater.*, 2018, **30**, 1801984.
19 A. Destefanis, S. Foglia and A. A. G. Tomlinson, *J. Mater. Chem.*, 1995, **5**, 475–483.
20 L. L. Peng, Y. Zhu, X. Peng, Z. W. Fang, W. S. Chu, Y. Wang, Y. J. Xie, Y. F. Li, J. J. Cha and G. H. Yu, *Nano Lett.*, 2017, **17**, 6273–6279.
21 R. F. De Farias and C. Airoldi, *Solid State Sci.*, 2003, **5**, 611–613.

22 N. Kinomura, T. Toyama and N. Kumada, *Solid State Ionics*, 1995, **78**, 281–286.
23 E. C. Zampronio and H. P. Oliveira, *Mater. Res. Bull.*, 2004, **39**, 1525–1538.
24 Z. Y. Wu, Y. N. Wang, L. Zhang, L. Jiang, W. C. Tian, C. L. Cai, J. Price, Q. F. Gu and L. F. Hu, *ACS Appl. Energy Mater.*, 2020, **3**, 3919–3927.
25 V. Verma, S. Kumar, W. Manalastas, J. Zhao, R. Chila, S. Z. Meng, P. Kidkhunthod and M. Srinivasan, *ACS Appl. Energy Mater.*, 2019, **2**, 8667–8674.
26 D. Kundu, B. D. Adams, V. Duffort, S. H. Vajargah and L. F. Nazar, *Nat. Energy*, 2016, **1**, 16119.
27 C. Xia, J. Guo, Y. J. Lei, H. F. Liang, C. Zhao and H. N. Alshareef, *Adv. Mater.*, 2018, **30**, 1705580.
28 P. He, M. Y. Yan, G. B. Zhang, R. M. Sun, L. N. Chen, Q. Y. An and L. Q. Mai, *Adv. Energy Mater.*, 2017, **7**, 1601920.
29 M. H. Alfaruqi, J. Gim, S. Kim, J. Song, D. T. Pham, J. Jo, Z. Xiu, V. Mathew and J. Kim, *Electrochem. Commun.*, 2015, **60**, 121–125.
30 Z. Y. Wu, C. J. Lu, Y. N. Wang, L. Zhang, L. Jiang, W. C. Tian, C. L. Cai, Q. F. Gu, Z. M. Sun and L. F. Hu, *Small*, 2020, **16**, 2000698.
31 H. Y. Shi, Y. J. Ye, K. Liu, Y. Song and X. Q. Sun, *Angew. Chem., Int. Ed.*, 2018, **57**, 16359–16363.
32 K. Ghanbari, M. F. Mousavi, M. Sharnsipur and H. Karami, *J. Power Sources*, 2007, **170**, 513–519.
33 H. Karami, M. F. Mousavi and M. Shamsipur, *J. Power Sources*, 2003, **117**, 255–259.
34 H. Z. Zhang, W. X. Wu, Q. Y. Liu, F. Yang, X. Shi, X. Q. Liu, M. H. Yu and X. H. Lu, *Angew. Chem., Int. Ed.*, 2021, **60**, 896–903.
35 I. S. Ahuja, D. H. Brown, R. H. Nuttall and D. W. A. Sharp, *J. Chem. Soc. A*, 1966, 938–941.
36 N. F. Quackenbush, L. Wangoh, D. O. Scanlon, R. Zhang, Y. Chung, Z. Chen, B. Wen, Y. Lin, J. C. Woicik, N. A. Chernova, S. P. Ong, M. S. Whittingham and L. F. J. Piper, *Chem. Mater.*, 2015, **27**, 8211–8219.
37 J. W. Ding, Z. G. Du, L. Q. Gu, B. Li, L. Z. Wang, S. W. Wang, Y. J. Gong and S. B. Yang, *Adv. Mater.*, 2018, **30**, 1800762.
38 M. Y. Yan, P. He, Y. Chen, S. Y. Wang, Q. L. Wei, K. N. Zhao, X. Xu, Q. Y. An, Y. Shuang, Y. Y. Shao, K. T. Mueller, L. Q. Mai, J. Liu and J. H. Yang, *Adv. Mater.*, 2018, **30**, 1703725.
39 D. Kundu, S. H. Vajargah, L. W. Wan, B. Adams, D. Prendergast and L. F. Nazar, *Energy Environ. Sci.*, 2018, **11**, 881–892.
40 V. Soundharrajan, B. Sambandam, S. Kim, M. H. Alfaruqi, D. Y. Putro, J. Jo, S. Kim, V. Mathew, Y. K. Sun and J. Kim, *Nano Lett.*, 2018, **18**, 2402–2410.
41 B. Y. Tang, G. Z. Fang, J. Zhou, L. B. Wang, Y. P. Lei, C. Wang, T. Q. Lin, Y. Tang and S. Q. Liang, *Nano Energy*, 2018, **51**, 579–587.
42 B. Sambandam, V. Soundharrajan, S. Kim, M. H. Alfaruqi, J. Jo, S. Kim, V. Mathew, Y. K. Sun and J. Kim, *J. Mater. Chem. A*, 2018, **6**, 3850–3856.
43 S. C. Liu, H. Zhu, B. H. Zhang, G. Li, H. K. Zhu, Y. Ren, H. B. Geng, Y. Yang, Q. Liu and C. C. Li, *Adv. Mater.*, 2020, **32**, 2001113.
44 B. Z. Jiang, C. J. Xu, C. L. Wu, L. B. Dong, J. Li and F. Y. Kang, *Electrochim. Acta*, 2017, **229**, 422–428.
45 N. Zhang, F. Y. Cheng, Y. C. Liu, Q. Zhao, K. X. Lei, C. C. Chen, X. S. Liu and J. Chen, *J. Am. Chem. Soc.*, 2016, **138**, 12894–12901.
46 W. B. Liu, J. W. Hao, C. J. Xu, J. Mou, L. B. Dong, F. Y. Jiang, Z. Kang, J. L. Wu, B. Z. Jiang and F. Y. Kang, *Chem. Commun.*, 2017, **53**, 6872–6874.
47 L. Y. Zhang, L. Chen, X. F. Zhou and Z. P. Liu, *Adv. Energy Mater.*, 2015, **5**, 1400930.
48 Z. Liu, G. Pulletikurthi and F. Endres, *ACS Appl. Mater. Interfaces*, 2016, **8**, 12158–12164.
49 Z. G. Hou, X. Q. Zhang, X. N. Li, Y. C. Zhu, J. W. Liang and Y. T. Qian, *J. Mater. Chem. A*, 2017, **5**, 730–738.
50 G. L. Li, Z. Yang, Y. Jiang, C. H. Jin, W. Huang, X. L. Ding and Y. H. Huang, *Nano Energy*, 2016, **25**, 211–217.
51 W. Li, K. L. Wang, S. J. Cheng and K. Jiang, *Energy Storage Mater.*, 2018, **15**, 14–21.
52 J. W. Zhao, Y. Q. Li, X. Peng, S. M. Dong, J. Ma, G. L. Cui and L. Q. Chen, *Electrochem. Commun.*, 2016, **69**, 6–10.
53 Q. Zhao, W. W. Huang, Z. Q. Luo, L. J. Liu, Y. Lu, Y. X. Li, L. Li, J. Y. Hu, H. Ma and J. Chen, *Sci. Adv.*, 2018, **4**, eaao1761.
54 D. Kundu, P. Oberholzer, C. Glaros, A. Bouzid, E. Tervoort, A. Pasquarello and M. Niederberger, *Chem. Mater.*, 2018, **30**, 3874–3881.
55 K. W. Nam, H. Kim, Y. Beldjoudi, T. W. Kwon, D. J. Kim and J. F. Stoddart, *J. Am. Chem. Soc.*, 2020, **142**, 2541–2548.
56 Z. W. Guo, Y. Y. Ma, X. L. Dong, J. H. Huang, Y. G. Wang and Y. Y. Xia, *Angew. Chem., Int. Ed.*, 2018, **57**, 11737–11741.
57 L. T. Ma, S. M. Chen, H. F. Li, Z. H. Ruan, Z. J. Tang, Z. X. Liu, Z. F. Wang, Y. Huang, Z. X. Pei, J. A. Zapien and C. Y. Zhi, *Energy Environ. Sci.*, 2018, **11**, 2521–2530.
58 B. Lee, C. S. Yoon, H. R. Lee, K. Y. Chung, B. W. Cho and S. H. Oh, *Sci. Rep.*, 2014, **4**, 6066.
59 C. J. Xu, B. H. Li, H. D. Du and F. Y. Kang, *Angew. Chem., Int. Ed.*, 2012, **51**, 933–935.
60 R. Trocoli and F. La Mantia, *ChemSusChem*, 2015, **8**, 481–485.
61 Y. X. Zeng, Z. Z. Lai, Y. Han, H. Z. Zhang, S. L. Xie and X. H. Lu, *Adv. Mater.*, 2018, **30**, 1802396.
62 Y. Gogotsi and R. M. Penner, *ACS Nano*, 2018, **12**, 2081–2083.
63 Y. Yan, B. Hao, D. Wang, G. Chen, E. Markweg, A. Albrecht and P. Schaaf, *J. Mater. Chem. A*, 2013, **1**, 14507–14513.
64 N. Zhang, Y. Dong, M. Jia, X. Bian, Y. Y. Wang, M. D. Qiu, J. Z. Xu, Y. C. Liu, L. F. Jiao and F. Y. Cheng, *ACS Energy Lett.*, 2018, **3**, 1366–1372.
65 S. S. Yao, J. Cui, Y. Deng, W. G. Chong, J. X. Wu, M. Ihsan-Ul-Haq, Y. W. Mai and J. K. Kim, *Energy Storage Mater.*, 2019, **20**, 36–45.
66 L. Jiang, Z. Y. Wu, Y. A. Wang, W. C. Tian, Z. Y. Yi, C. L. Cai, Y. C. Jiang and L. F. Hu, *ACS Nano*, 2019, **13**, 10376–10385.

67 F. H. Yang, J. Hong, J. N. Hao, S. L. Zhang, G. M. Liang, J. Long, Y. Q. Liu, N. N. Liu, W. K. Pang, J. Chen and Z. P. Guo, *Adv. Energy Mater.*, 2020, **10**, 1903826.
68 N. Zhang, F. Y. Cheng, J. X. Liu, L. B. Wang, X. H. Long, X. S. Liu, F. J. Li and J. Chen, *Nat. Commun.*, 2017, **8**, 405.
69 Q. C. Zhuang, T. Wei, L. L. Du, Y. L. Cui, L. Fang and S. G. Sun, *J. Phys. Chem. C*, 2010, **114**, 8614–8621.
70 N. Dupre, J. Gaubicher, T. Le Mercier, G. Wallez, J. Angenault and M. Quarton, *Solid State Ionics*, 2001, **140**, 209–221.

